

Antarctic shelf ocean warming and sea ice melt affected by projected El Niño changes

Article

Published Version

Creative Commons: Attribution 4.0 (CC-BY)

Open Access

Cai, W., Jia, F., Li, S., Purich, A., Wang, G., Wu, L., Gan, B., Santoso, A., Geng, T., Ng, B., Yang, Y., Ferreira, D. ORCID: <https://orcid.org/0000-0003-3243-9774>, Meehl, G. A. and McPhaden, M. (2023) Antarctic shelf ocean warming and sea ice melt affected by projected El Niño changes. *Nature Climate Change*, 13. pp. 235-239. ISSN 1758-678X doi: <https://doi.org/10.1038/s41558-023-01610-x> Available at <https://centaur.reading.ac.uk/109906/>

It is advisable to refer to the publisher's version if you intend to cite from the work. See [Guidance on citing](#).

To link to this article DOI: <http://dx.doi.org/10.1038/s41558-023-01610-x>

Publisher: Nature Publishing Group

All outputs in CentAUR are protected by Intellectual Property Rights law, including copyright law. Copyright and IPR is retained by the creators or other copyright holders. Terms and conditions for use of this material are defined in the [End User Agreement](#).

www.reading.ac.uk/centaur

CentAUR

Central Archive at the University of Reading

Reading's research outputs online



Antarctic shelf ocean warming and sea ice melt affected by projected El Niño changes

Received: 19 September 2022

Accepted: 18 January 2023

Published online: 20 February 2023

 Check for updates

Wenju Cai ^{1,2,3}✉, Fan Jia ⁴, Shujun Li ^{1,2}, Ariaan Purich ^{5,6}, Guojian Wang ^{1,2,3}, Lixin Wu ^{1,2}✉, Bolan Gan ^{1,2}, Agus Santoso ^{3,7}, Tao Geng ², Benjamin Ng ³, Yun Yang ⁸, David Ferreira ⁹, Gerald A. Meehl ¹⁰ & Michael J. McPhaden ¹¹

Antarctic shelf ocean warming affects melt of ice shelf/sheets and sea ice but projected changes vary vastly across climate models. A projected increase in El Niño variability has been found to slow future mid-latitude Southern Ocean warming but how this impacts the Antarctic shelf ocean is unknown. Here we show that a projected increase in El Niño variability accelerates Antarctic shelf ocean warming, hastening ice shelf/sheet melt but slowing sea ice reduction.

Around Antarctica (poleward -60° S), ocean below 200 m is warmer than the surface ocean¹. This inversion in vertical temperature profile is not present north of -60° S (see ‘Observations’ in Methods) (Extended Data Fig. 1). Southern high-latitude winds drive divergent surface flows that draw water up from below^{2–6}. Most of the water upwells from a depth of 2–3 km along sloping density layers with little heat input or mixing required⁷. Upon surfacing, the upwelled waters split into two branches⁸. One flows equatorward (northward -60° S) where the upwelled water is cooler than the ambient ocean and atmosphere and is heated by the atmosphere before eventual subduction into the mid-latitude ocean interior, ensuring that the Southern Ocean takes a large portion of the excess heat from greenhouse warming. The other branch is located poleward -60° S where the upwelled water is warmer than the ambient ocean and air temperatures and loses heat to the atmosphere, affecting sea ice formation. Imprints of the importance of the warm upwelling are highlighted in a heat budget analysis, showing that air–sea heat flux cools the ocean and the warm upwelling heats the shelf and surface waters (Extended Data Fig. 2).

Observed warming of the Southern Ocean shows a rich vertical structure around Antarctica. Pan-Antarctic surface water has cooled and Antarctic sea ice has increased during the 1979–2015 period^{9,10}. In a sharp contrast, the Antarctic shelf ocean waters (waters above

the seabed with bathymetry shallower than 1,500 m) in the Amundsen and Bellingshausen Seas have warmed substantially^{10–13}. Consequently, West Antarctic ice shelves and ice sheet have lost substantial mass between 1992 and 2017, particularly from the Pine Island and Thwaites Glacier catchments of the Amundsen Sea Embayment^{14,15}. The warming of shelf ocean water critically affects the pace of Antarctic ice shelf and ice sheet melt¹¹. Under greenhouse warming, heating from warm upwelling intensifies but varies vastly across models¹⁶.

A projected increase in El Niño–Southern Oscillation (ENSO) variability is found to slow mid-latitude Southern Ocean warming¹⁷. During El Niño, including central-Pacific El Niño¹⁸, tropical convective anomalies induce a Pacific South American pattern of anomalies and an equatorward contraction of the Hadley, Ferrell and Polar cells, generating zonally symmetric high-latitude easterly anomalies^{17,18}. During La Niña, the reverse occurs. Because El Niño warm anomalies and the teleconnections are overall greater than those of La Niña cold anomalies¹⁹, over several ENSO cycles, there are anticyclonic circulation anomalies over the Amundsen and Bellingshausen Seas but easterly anomalies over much of the southern high latitudes¹⁷. Due to this ENSO rectifying effect, models that project a greater increase in ENSO variability systematically generate a weaker westerly poleward intensification over the southern high latitudes. The associated smaller

¹Frontier Science Centre for Deep Ocean Multispheres and Earth System and Physical Oceanography Laboratory, Ocean University of China, Qingdao, China. ²Laoshan Laboratory, Qingdao, China. ³Centre for Southern Hemisphere Oceans Research (CSHOR), CSIRO Oceans and Atmosphere, Hobart, Australia. ⁴CAS Key Laboratory of Ocean Circulation and Waves, Institute of Oceanology, Chinese Academy of Sciences, Qingdao, China. ⁵School of Earth, Atmosphere and Environment, Monash University, Melbourne, Australia. ⁶ARC Special Research Initiative for Securing Antarctica’s Environmental Future, Melbourne, Australia. ⁷Australian Research Council (ARC) Centre of Excellence for Climate Extremes, The University of New South Wales, Sydney, Australia. ⁸College of Global Change and Earth System Science, Beijing Normal University, Beijing, China. ⁹Department of Meteorology, University of Reading, Reading, UK. ¹⁰Climate and Global Dynamics Laboratory, National Center for Atmospheric Research, Boulder, CO, USA. ¹¹NOAA Pacific Marine Environmental Laboratory (PMEL), Seattle, WA, USA. ✉e-mail: Wenju.Cai@csiro.au; lxwu@ouc.edu.cn

increase in circum-Antarctic upwelling leads to the slower mid-latitude Southern Ocean warming¹⁷. However, how the ENSO response affects Antarctic shelf ocean is unknown.

Here we show that a greater increase in future ENSO variability accelerates Antarctic shelf ocean warming but slows surface warming around sea ice edges. Models that simulate a greater increase in ENSO variability systematically generate an accelerated circum-Antarctic shelf ocean warming but slowed surface temperature increases, with important implications.

We examine 31 climate models that participated in Phase 6 of the Coupled Model Intercomparison Project²⁰ (CMIP6) under historical forcings before 2014 and a high-emission scenario (that is, Shared Socioeconomic Pathways (SSP) 5–8.5) (see ‘CMIP6 outputs’ in Methods and Supplementary Table 1). These models simulate the observed feature of the high-latitude temperature structure, which persists into the twenty-first century (Extended Data Fig. 3). In addition, models simulate reasonably well the dominant variability patterns, their link to ENSO through the Pacific South American pattern^{21–23} and the zonally symmetric meridional anomalies¹⁷.

Multimodel mean change, defined as the difference between the twenty-first (2000–2099) and the twentieth (1900–1999) century, features a westerly poleward intensification, an increase in the associated negative wind stress curls around Antarctica, a reduction in Antarctic sea ice concentration and zonally averaged Southern Ocean warming with a maximum centred around 45° S (Extended Data Fig. 4); poleward 60° S, as greenhouse warming proceeds, atmospheric cooling of the warm upwelled water weakens. However, the warm upwelling increases such that even by 2100, the ocean poleward 60° S still loses heat to the atmosphere (Extended Data Fig. 5).

We use Niño3.4 (5° S–5° N, 170° W–120° W) sea surface temperature (SST) index in the ENSO matured season of December, January, February (DJF) to describe ENSO (see ‘ENSO response’ in Methods). Monthly SST anomalies over 1900–2099 are constructed with reference to the climatology over the 1900–1999 period and quadratically detrended. Zonally averaged shelf ocean temperatures are constructed by shifting the latitude^{16,24} relative to the 1,000 m isobath at each longitude before zonal averaging (see ‘Zonal mean of shelf ocean temperatures’ in Methods). To examine inter-model relationships, changes are scaled by the increase of global mean SST in each model (last column, Supplementary Table 1) to remove impact from climate sensitivity.

A greater increase in ENSO variability is systematically linked to a faster shelf ocean warming but to a slower surface warming around the sea ice edge (Fig. 1a) that in turn slows sea ice melt (Fig. 1b). The linkage is seen in an inter-model correlation of ENSO changes with sea ice changes averaged over the 60° S–70° S circumpolar band ($r = 0.70$) (Fig. 1c) and with averaged shelf ocean warming over 400–1,500 m near the shelf break ($r = 0.63$) (area confined by black thick line, Fig. 1c), or horizontally (Fig. 1d). The averaged shelf ocean warming reflects warming at various depth ranges including the upper 200–400 m (Extended Data Fig. 6). A large inter-model spread exists in the projected changes, but the inter-model correlation amplitude suggests that the inter-model differences in ENSO changes account

for approximately 40% (r^2) of the spread in the shelf ocean warming, and approximately 45% of the spread in sea ice reduction.

A total of 23 out of 31 (74%) models generate an increased ENSO amplitude with a multimodel mean increase of -11.4% , consistent with a recent finding²⁵. The overall increase in ENSO variability accelerates Antarctic shelf ocean warming but slows sea ice reduction. Below we show that the impact of ENSO change is effected via the circum-Antarctic warm upwelling.

Based on a dynamically consistent ocean–atmosphere reanalysis over the 1979–2018 period, poleward 60° S, grid-point upwelling values at 100 m can be approximated by wind-driven Ekman upwelling values with a correlation of 0.86. Thus, we use wind-driven Ekman upwelling and modelled grid-point vertical temperatures at 100 m to calculate changes in heating from warm upwelling, as in previous studies²⁶.

In models with a larger increase in ENSO amplitude, ENSO-induced easterly anomalies are greater over much of Antarctica. The difference in the ENSO-rectified winds is seen in an inter-model relationship, or in a comparison between the top five models that produce the largest ENSO increase and the bottom five models that simulate the smallest ENSO change (Extended Data Fig. 7). In the top five models, as the rectified easterlies offset the westerly poleward intensification, the increase in circum-Antarctic warm upwelling is rather small (Fig. 1e), except in the Amundsen and Bellingshausen Seas. In the bottom five models, the increase in circum-Antarctic warm upwelling is large and little affected by ENSO change. The difference between the two groups of models is statistically significant (stippled areas in Fig. 1f) but not exactly zonally symmetric, suggesting that the change due to the Pacific South American teleconnection modifies the zonal-symmetric pattern. In models with a greater ENSO increase, because relatively less of the shelf ocean warm water is transported to the surface, shelf ocean warming accelerates but surface warming slows. Through this process, a greater increase in ENSO variability leads to a slower sea ice reduction despite a larger heating from the atmosphere (Extended Data Fig. 8).

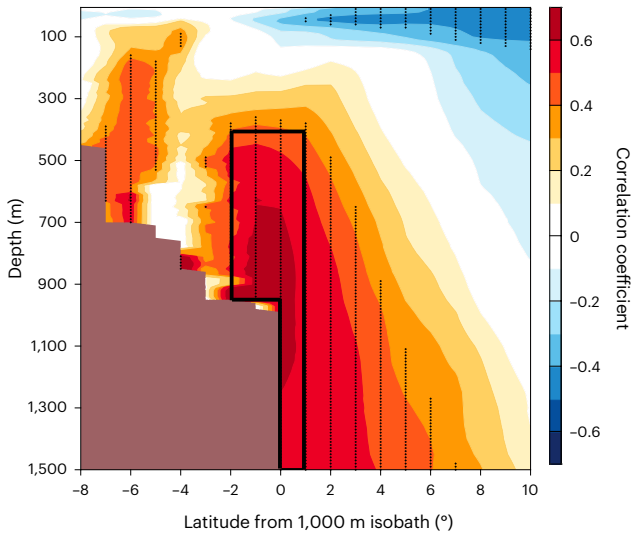
The role of the changing circum-Antarctic warm upwelling in affecting shelf ocean warming and sea ice melt is confirmed in a multivariate empirical orthogonal function²⁷ (MV-EOF) analysis on modelled changes, all scaled by the increase in global mean SST in each model. The first principal pattern depicts their dominant covarying changes, regardless of how the changes are driven, and the associated first principal component (PC1) indicates the inter-model differences. The process discussed above emerges as a smaller increase in Antarctic warm upwelling generates a faster Antarctic shelf ocean warming, which would favour a faster ice shelf and ice sheet melt, but a slower warming in the surface ocean that is conducive to a slower sea ice reduction (Fig. 2a–c). The role of the projected ENSO changes is reflected in an inter-model correlation of $r = 0.68$ between ENSO changes and MV-EOF PC1 (Fig. 2d).

In summary, the projected twenty-first century enhancement in ENSO variability probably accelerates Antarctic shelf ocean warming and ice shelf and ice sheet melt, but slows surface warming around sea ice edge and sea ice reduction. This impact from projected increase in ENSO variability is exerted by moderating the high-latitude poleward westerly intensification, ultimately reducing the increase in

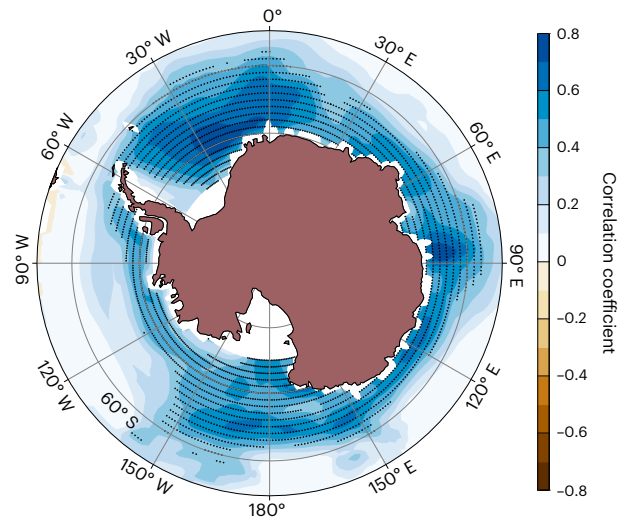
Fig. 1 | Enhanced ENSO slows sea ice melt but hastens shelf ocean warming by suppressing warm upwelling. a–c, Inter-model correlation of changes in ENSO variability ($^{\circ}\text{C }^{\circ}\text{C}^{-1}$ of global warming) with zonally averaged shelf water temperature ($^{\circ}\text{C }^{\circ}\text{C}^{-1}$ of global warming) (a), sea ice concentration (SIC) changes ($\% ^{\circ}\text{C}^{-1}$ of global warming) (b), and an averaged Antarctic shelf water warming (black box in a) and sea ice changes averaged over the 60° S–70° S latitude band (c). d, Inter-model correlation of the averaged Antarctic shelf water warming with ENSO variability changes, both scaled by global warming in each model. In a, the latitude is shifted relative to the 1,000 m isobath (green curve in d) at each longitude before zonal averaging (see ‘Zonal mean of shelf ocean temperatures’

in Methods). In c, linear fits are displayed together with the correlation coefficient r and P value; dotted areas in a, b and d indicate statistical significance above the 95% confidence level determined by a two-sided Student’s t -test. e, f, Projected change in heating from upwelling ($^{\circ}\text{C s}^{-1} ^{\circ}\text{C}^{-1}$ of global warming) averaged over the top five models with greatest ENSO variability increase (e), and over the bottom five models with smallest ENSO variability change (f). Dotted areas in f indicate where the differences between e and f are statistically significant above the 95% confidence level as determined by a two-sided Student’s t -test.

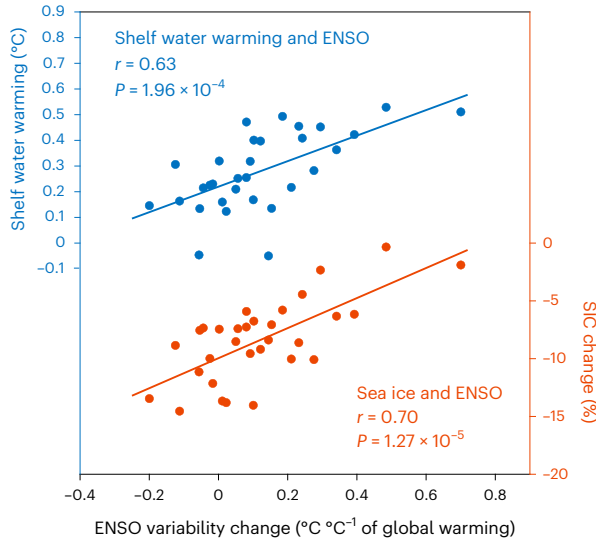
a Correlation between changes in ENSO and temperature



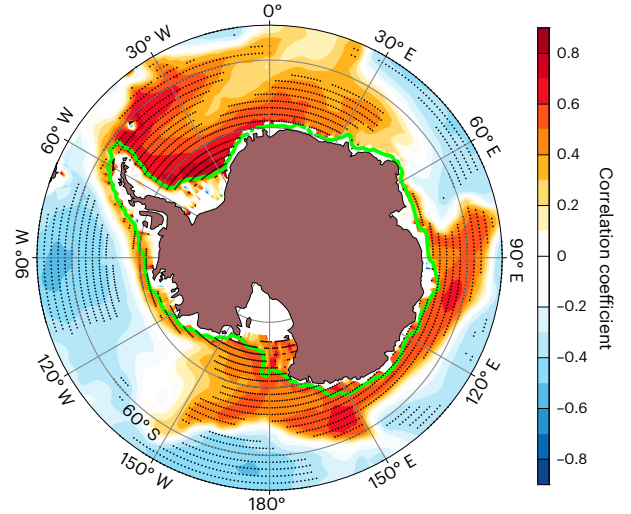
b Change in SIC and ENSO variability



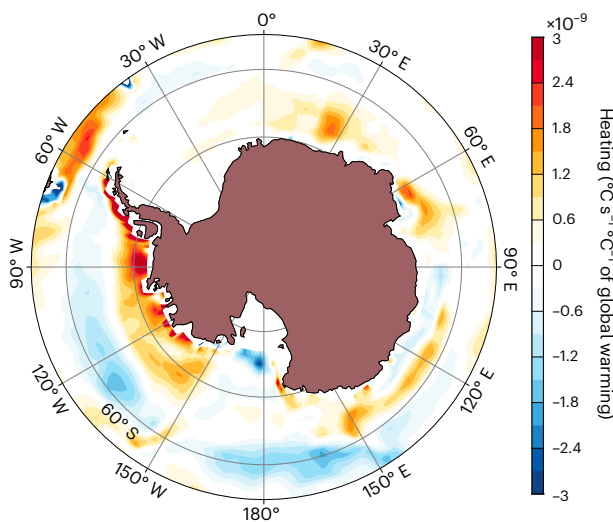
c Inter-model correlation



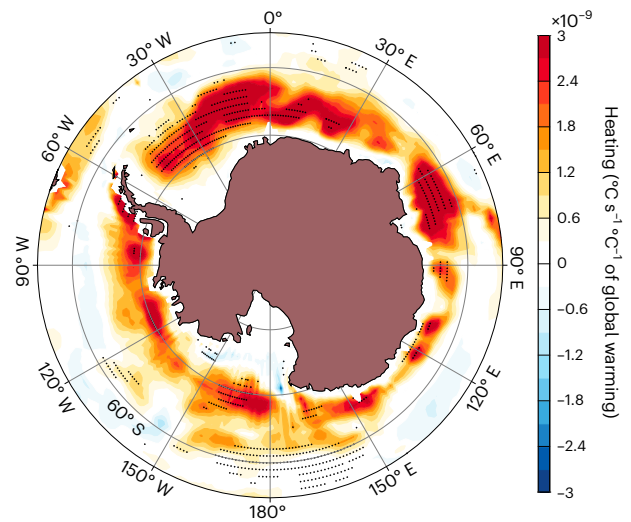
d Change in temperature (400–1,500 m) and ENSO variability



e Change in heating from upwelling with large ENSO response



f Change in heating from upwelling with small ENSO response



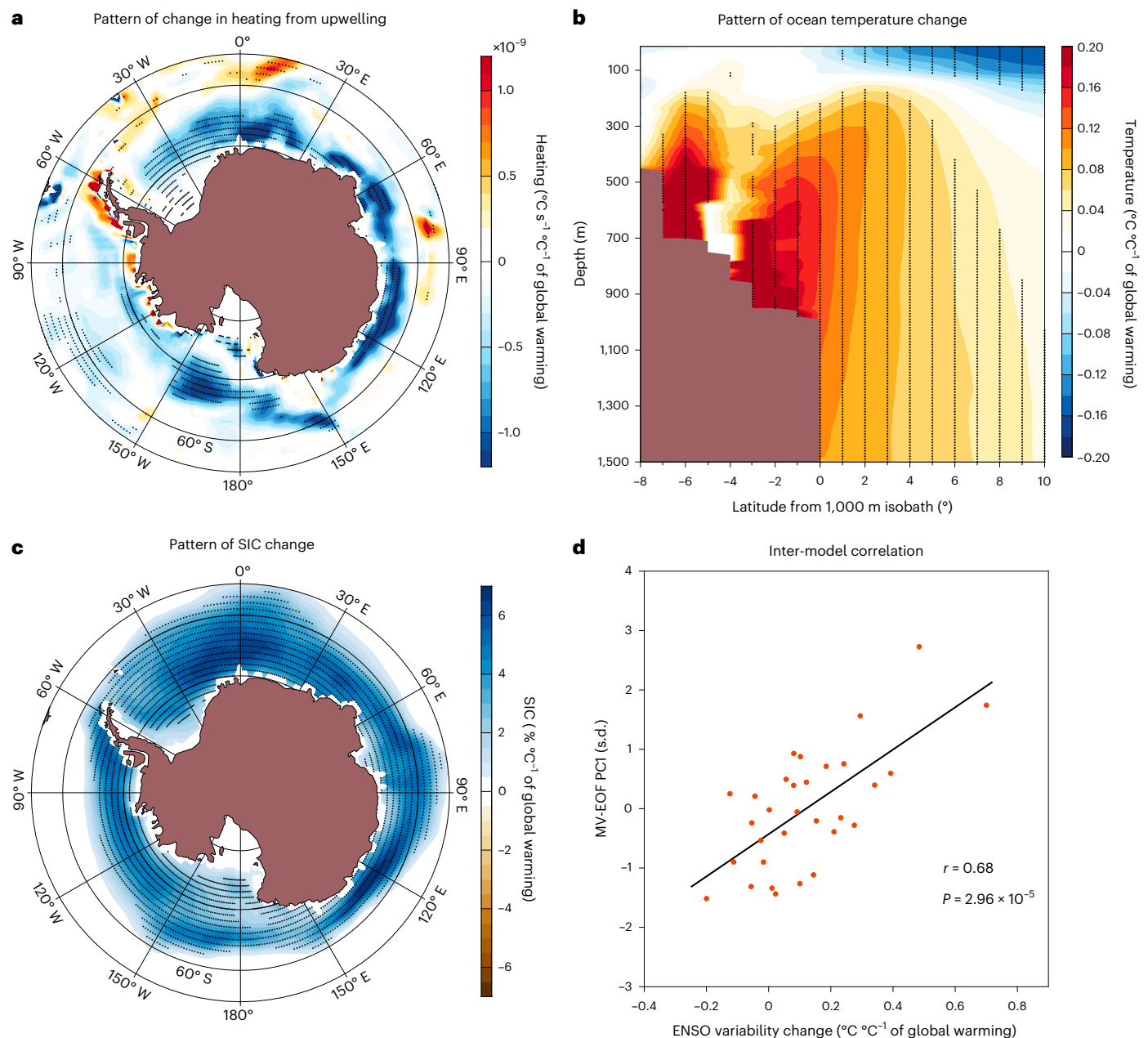


Fig. 2 | Reduced warm upwelling accelerates shelf ocean warming but slows surface warming. **a–c**, Shown are the first principal pattern of a multivariate EOF (MV-EOF) analysis of inter-model differences in projected changes in the domain poleward of 55°S from the twentieth century to the twenty-first century of heating of the surface layer from warm upwelling ($^{\circ}\text{C s}^{-1} \text{ } ^{\circ}\text{C}^{-1}$ of global warming) (**a**), zonally averaged shelf water temperatures ($^{\circ}\text{C } ^{\circ}\text{C}^{-1}$ of global warming) (**b**)

and SIC ($\% \text{ } ^{\circ}\text{C}^{-1}$ of global warming) in the domain south of 55°S (**c**). **d**, Inter-model relationship between the associated principal component (PCI, s.d.) and ENSO variability change ($^{\circ}\text{C } ^{\circ}\text{C}^{-1}$ of global warming); a linear fit is displayed together with the correlation coefficient r and the P value. Dotted areas in **a–c** indicate regression coefficients that are statistically significant above the 95% confidence level as determined by a two-sided Student's t -test.

circum-Antarctic warm upwelling. Thus, implications of the projected increase in ENSO variability transcend risks of extreme weathers²⁸ and extend into impacts on changing Antarctic sea ice and Antarctic ice shelf and ice sheet.

Online content

Any methods, additional references, Nature Portfolio reporting summaries, source data, extended data, supplementary information, acknowledgements, peer review information; details of author contributions and competing interests; and statements of data and code availability are available at <https://doi.org/10.1038/s41558-023-01610-x>.

References

- Roemmich, D. & Gilson, J. The 2004–2008 mean and annual cycle of temperature, salinity, and steric height in the global ocean from the Argo Program. *Prog. Oceanogr.* **82**, 81–100 (2009).
- Armour, K. C., Marshall, J., Scott, J. R., Donohoe, A. & Newsom, E. R. Southern Ocean warming delayed by circumpolar upwelling and equatorward transport. *Nat. Geosci.* **9**, 549–554 (2016).
- Cai, W., Cowan, T., Godfrey, S. & Wijffels, S. Simulations of processes associated with the fast-warming rate of the southern midlatitude ocean. *J. Clim.* **23**, 197–206 (2010).

4. Swart, N. C., Gille, S. T., Fyfe, J. C. & Gillett, N. P. Recent Southern Ocean warming and freshening driven by greenhouse gas emissions and ozone depletion. *Nat. Geosci.* **11**, 836–841 (2018).
5. Exarchou, E., Kuhlbrodt, T., Gregory, J. & Smith, R. Ocean heat uptake processes: a model intercomparison. *J. Clim.* **28**, 887–908 (2015).
6. Morrison, A., Griffies, S., Winton, M., Anderson, W. & Sarmiento, J. Mechanisms of southern ocean heat uptake and transport in a global eddying climate model. *J. Clim.* **29**, 2059–2075 (2016).
7. Wolfe, C. L. & Cessi, P. The adiabatic pole-to-pole overturning circulation. *J. Phys. Oceanogr.* **41**, 1795–1810 (2011).
8. Marshall, J. & Speer, K. Closure of the meridional overturning circulation through Southern Ocean upwelling. *Nat. Geosci.* **5**, 171–180 (2012).
9. Holland, P. R. The seasonality of Antarctic sea ice trends. *Geophys. Res. Lett.* **41**, 4230–4237 (2014).
10. Li, X. et al. Tropical teleconnection impacts on Antarctic climate changes. *Nat. Rev. Earth Environ.* **2**, 680–698 (2021).
11. Schmidtko, S. et al. Multidecadal warming of Antarctic waters. *Science* **334**, 1227–1231 (2014).
12. Cook, A. J. et al. Ocean forcing of glacier retreat in the western Antarctic Peninsula. *Science* **353**, 283–286 (2016).
13. Pritchard, H. D. et al. Antarctic ice-sheet loss driven by basal melting of ice shelves. *Nature* **484**, 502–505 (2012).
14. Shepherd, A. et al. Mass balance of the Antarctic Ice Sheet from 1992 to 2017. *Nature* **558**, 219–222 (2018).
15. Wouters, B. et al. Dynamic thinning of glaciers on the Southern Antarctic Peninsula. *Science* **348**, 899–903 (2015).
16. Purich, A. & England, M. H. Historical and future projected warming of Antarctic shelf bottom water in CMIP6 models. *Geophys. Res. Lett.* **48**, e2021GL092752 (2021).
17. Wang, G. et al. Future Southern Ocean warming linked to projected ENSO variability. *Nat. Clim. Change* **12**, 649–654 (2022).
18. Zhang, C., Li, T. & Li, S. Impacts of CP and EP El Niño events on the Antarctic sea ice in austral spring. *J. Clim.* **34**, 9327–9348 (2021).
19. Dommenget, D., Bayr, T. & Frauen, C. Analysis of the non-linearity in the pattern and time evolution of El Niño Southern Oscillation. *Clim. Dyn.* **40**, 2825–2847 (2013).
20. Eyring, V. et al. Overview of the Coupled Model Intercomparison Project Phase 6 (CMIP6) experimental design and organization. *Geosci. Model Dev.* **9**, 1937–1958 (2016).
21. Li, S., Cai, W. & Wu, L. Weakened Antarctic dipole under global warming in CMIP6 models. *Geophys. Res. Lett.* **48**, e2021GL094863 (2021).
22. Turner, J. The El Niño–Southern Oscillation and Antarctica. *Int. J. Clim.* **24**, 1–31 (2004).
23. Welhouse, L. J., Lazzara, M. A., Keller, L. M., Tripoli, G. J. & Hitchman, M. H. Composite analysis of the effects of ENSO events on Antarctica. *J. Clim.* **29**, 1797–1808 (2016).
24. Little, C. M. & Urban, N. M. CMIP5 temperature biases and 21st century warming around the Antarctic coast. *Ann. Glaciol.* **57**, 69–78 (2016).
25. Cai, W. et al. Increased ENSO sea surface temperature variability under four IPCC emission scenarios. *Nat. Clim. Change* **12**, 228–231 (2022).
26. Meehl, G. A. et al. Sustained ocean changes contributed to sudden Antarctic sea ice retreat in late 2016. *Nat. Commun.* **10**, 14 (2019).
27. Wang, B. The vertical structure and development of the ENSO anomaly mode during 1979–1989. *J. Atmos. Sci.* **49**, 698–712 (1992).
28. Cai, W. et al. Changing El Niño–Southern Oscillation in a warming climate. *Nat. Rev. Earth Environ.* **2**, 628–644 (2021).

Publisher's note Springer Nature remains neutral with regard to jurisdictional claims in published maps and institutional affiliations.

Open Access This article is licensed under a Creative Commons Attribution 4.0 International License, which permits use, sharing, adaptation, distribution and reproduction in any medium or format, as long as you give appropriate credit to the original author(s) and the source, provide a link to the Creative Commons license, and indicate if changes were made. The images or other third party material in this article are included in the article's Creative Commons license, unless indicated otherwise in a credit line to the material. If material is not included in the article's Creative Commons license and your intended use is not permitted by statutory regulation or exceeds the permitted use, you will need to obtain permission directly from the copyright holder. To view a copy of this license, visit <http://creativecommons.org/licenses/by/4.0/>.

© The Author(s) 2023

Methods

Observations

We used ocean temperature data from Argo gridded data¹ since 2004 to examine the vertical temperature structures and their changes over time (Extended Data Fig. 2), and SSTs from the Hadley Centre Sea Ice and SST dataset (HadISST) (ref.²⁹) to examine the observed ENSO property. Monthly fields were used and, where needed, anomalies were calculated with reference to the monthly climatology over the full period (1979–2018) and quadratically detrended.

We used surface heat fluxes and winds from six products for a multiproduct average, and these products included the National Centre for Environmental Prediction (NCEP)/National Centre for Atmospheric Research (NCAR) reanalysis I (1.9° latitude and 1.875° longitude) (ref.³⁰), the fifth generation European Centre for Medium-Range Weather Forecasts (ECMWF) reanalysis for the global climate and weather (ERA5; 0.25° grid) (ref.³¹), the Japanese 55 year Reanalysis (JRA-55; 1.25° grid) (ref.³²), the Modern-Era Retrospective Analysis for Research and Applications Version 2 (MERRA2; 0.5° latitude and 0.625° longitude) (ref.³³), and the combination of NCEP Climate Forecast System Reanalysis (CFSR; 1979–2010; -0.31° grid) (ref.³⁴) and the NCEP Climate Forecast System Version 2 (CFSV2; 2011–2020; -0.2° grid) (ref.³⁵). Each field was re-gridded onto a common 1° × 1° resolution before averaging across products. Together with ECMWF three-dimensional monthly fields of Ocean Reanalysis System 5 (ORAS5; 0.25° grid) (ref.³⁶) over the 1979–2018 period, the multiproduct averaged winds were used to reveal the imprints of two Southern Ocean upwelling pathways on temperature as shown in Extended Data Fig. 2a–c.

We used the oceanic circulation fields from ORAS5 (ref.³⁶) over the 1979–2018 period to conduct a full heat budget analysis over the upper 100 m poleward 60° S (Extended Data Fig. 2d). The heat budget is described by

$$\frac{\partial T_m}{\partial t} = -V \frac{\partial T}{\partial y} - W \frac{\partial T}{\partial z} + \frac{\text{NHF}}{\rho_0 C_p H} + R \quad (1)$$

where T_m is average temperature over the upper 100 m; $-V \frac{\partial T}{\partial y}$ is meridional advection averaged over the upper 100 m; $-W \frac{\partial T}{\partial z}$ is vertical advection across the 100 m depth; $\frac{\text{NHF}}{\rho_0 C_p H}$ is atmospheric heating/cooling from net heat flux (NHF) averaged over the six analysis products, in which ρ_0 is the density of seawater taken as 1,025 kg m⁻³, C_p the heat capacity of seawater taken as 4,200 J kg⁻¹ K⁻¹, H is the ocean upper layer depth taken as 100 m and R is the residual which includes zonal advection, mixing and diffusive terms. The vertical gradient $\frac{\partial T}{\partial z}$ was calculated as the difference between averages over the 70–100 m and 100–130 m depth. The regional average poleward 60° S over the period shows that atmospheric cooling (referred to as $Q = \frac{\text{NHF}}{\rho_0 C_p H}$) and cooling due to meridional advection (referred to as F_v) are largely balanced by heating from warm upwelling (referred to as F_w).

A comparison of oceanic currents with those inferred from wind-driven Ekman flows shows that upwelling across the 100 m depth and meridional currents across 60° S are highly correlated with the wind-driven Ekman upwelling $W_e = (\nabla \times \frac{\tau}{\rho f})$ and Ekman velocity $V_e = -\frac{\tau_x}{Hf\rho}$, respectively, with a correlation of 0.86 and 0.95. Here, τ_x is the grid-point zonal wind stress; f is the Coriolis parameter calculated as $2\Omega \sin(\theta)$, where Ω is the rotation rate of the planet and θ is latitude (f is negative in the Southern Hemisphere). As such, we examined heating associated with Ekman flows in climate models.

CMIP6 outputs

We took monthly outputs of ocean and atmosphere fields from 31 CMIP6 models in which data are available for ocean temperature, surface wind stress, heat flux (latent heat flux from Korea Institute of

Ocean Science and Technology Earth System Model was unavailable) and Antarctic sea ice concentration. These models were forced under historical forcings (1850–2014) and the SSP5–8.5 (2015–2100) emission scenario²⁰ (see Supplementary Table 1 for details). Before data analysis, outputs of each model were re-gridded onto a common 1° × 1° resolution. For ocean temperatures, the common vertical levels from the surface to 5,000 m were on a 5 m increment.

The projected change in heating from warm upwelling was calculated as the difference between averages over the 2000–2099 (twenty-first century) and the 1900–1999 (twentieth century) periods. Change in heating from warm upwelling was calculated as $-\Delta \left(\nabla \times \frac{\tau}{\rho f} \right) \frac{dT}{dz}$ between the twenty-first and twentieth centuries; $\frac{dT}{dz}$ is the grid-point climatological vertical temperature gradient. The gradient was calculated as the difference between temperature averaged over 50–100 m and that averaged over 100–150 m. Using averages over different depth ranges leads to similar results.

ENSO response

We used the conventional Niño3.4 index for ENSO, which is defined as the SST anomaly in the central-eastern equatorial Pacific (5° S–5° N, 170° W–120° W). Monthly SST anomalies were constructed with reference to the climatology over the 1900–1999 period and quadratically detrended. We calculated the change in ENSO variability as the difference between the twenty-first and twentieth centuries in the standard deviation of the Niño3.4 index during the ENSO peak season (DJF). Similarly, the change was scaled by °C⁻¹ of global mean SST warming.

Zonal mean of shelf ocean temperatures

Conventional zonal average of ocean temperatures could lead to averages over the open ocean and near-shelf areas, rather than the shelf ocean only. To overcome this issue, we used an approach employed in previous studies^{16,24} in which the latitude is shifted relative to the 1,000 m isobath at each longitude before zonal averaging. That is, the 1,000 m isobath was used as a reference point to composite the temperature offshore and onshore from this point around the Antarctic shelf³⁷. This allowed the Antarctic shelf to be clearly seen in adjusted latitudes south of the 1,000 m isobath (that is, negative x axis), and the bottom shelf and open ocean to be averaged north of the 1,000 m isobath (that is, positive x axis).

Data availability

Data related to the paper can be downloaded from the following:

- NCEP/NCAR data, <https://www.esrl.noaa.gov/psd/data/gridded/data.ncep.reanalysis.derived.html>;
- ERA5 data, <https://www.ecmwf.int/en/forecasts/datasets/reanalysis-datasets/era5>;
- JRA-55 data, https://jra.kishou.go.jp/JRA-55/index_en.html;
- MERRA2 data, https://gmao.gsfc.nasa.gov/reanalysis/MERRA-2/data_access/;
- NCEP CFSR data, <https://rda.ucar.edu/datasets/ds093.2/>;
- NCEP CFSv2 data, <https://rda.ucar.edu/datasets/ds094.2/>;
- HadISST v1.1, <https://www.metoffice.gov.uk/hadobs/hadisst/>;
- Argo gridded data by Scripps, http://sio-argo.ucsd.edu/RG_Climatology.html;
- ORAS5 data, <https://www.cen.uni-hamburg.de/en/icdc/data/ocean/easy-init-ocean/ecmwf-oras5.html>;
- CMIP6 database, <https://esgf-node.llnl.gov/projects/cmip6/>.

Code availability

Codes for calculating MV-EOF and shelf water temperatures are publicly available via Zenodo at <https://doi.org/10.5281/zenodo.7524259> (ref.³⁷). Codes for calculating correlation and regression are available from the corresponding authors on request.

References

29. Rayner, N. A. et al. Global analyses of sea surface temperature, sea ice, and night marine air temperature since the late nineteenth century. *J. Geophys. Res.* **108**, 4407 (2003).
30. Kalnay, E. et al. The NCEP/NCAR 40-year reanalysis project. *Bull. Am. Meteorol. Soc.* **77**, 437–471 (1996).
31. Hersbach, H. et al. *ERA5 Monthly Averaged Data on Single Levels from 1959 To Present* (Copernicus Climate Change Service Climate Data Store, 2019).
32. Kobayashi, S. et al. The JRA-55 reanalysis: general specifications and basic characteristics. *J. Meteorol. Soc. Jpn.* **93**, 5–48 (2015).
33. Gelaro, R. et al. The modern-era retrospective analysis for research and applications, Version 2 (MERRA-2). *J. Clim.* **30**, 5419–5454 (2017).
34. Saha, S. et al. The NCEP climate forecast system reanalysis. *Bull. Am. Meteorol. Soc.* **91**, 1015–1058 (2010).
35. Saha, S. et al. The NCEP climate forecast system version 2. *J. Clim.* **27**, 2185–2208 (2014).
36. Zuo, H., Balmaseda, M. A., Tietsche, S., Mogensen, K. & Mayer, M. The ECMWF operational ensemble reanalysis-analysis system for ocean and sea ice: a description of the system and assessment. *Ocean Sci.* **15**, 779–808 (2019).
37. JIA, F. MATLAB code for calculating MVEOF and shelf water temperatures. *Zenodo* <https://doi.org/10.5281/zenodo.7524259> (2023).

Acknowledgements

This work was supported by the National Key Research and Development Program of China 2018YFA0605700, the Science and Technology Innovation Project of Laoshan Laboratory (LSKJ202203302, LSKJ202202402), the Strategic Priority Research Program of the Chinese Academy of Sciences (grant XDB40030000) and the Centre for Southern Hemisphere Oceans Research, a joint research centre between QNLM and CSIRO. F.J. was supported by the National Key Research and Development Program of China 2020YFA0608801, National Natural Science Foundation of China (NSFC) projects (41876008, 41730534) and Youth Innovation Promotion Association of the Chinese Academy of Sciences (2021205). S.L. was supported by the National Natural Science Foundation of China (NSFC) project 42006173 and the National Key Research and Development Program of China 2019YFC1509102. A.P. was supported by the Australian Research Council Special Research Initiative for Securing Antarctica's Environmental Future (SR200100005). G.W., B.N. and A.S. were supported by the Earth

Systems and Climate Change Hub of the Australian Government's National Environmental Science Program. T.G. was supported by the NSFC project (2206209) and the China National Postdoctoral Program for Innovative Talents (BX20220279). PMEL contribution no. 5447. G.A.M. was supported by the Regional and Global Model Analysis (RGMA) component of the Earth and Environmental System Modeling Program of the US Department of Energy's Office of Biological and Environmental Research (BER) via National Science Foundation IA 1844590 and under Award Number DE-SC0022070, and also by the National Center for Atmospheric Research, which is a major facility sponsored by the National Science Foundation (NSF) under Cooperative Agreement No. 1852977. Open access funding provided by CSIRO Library Services. We thank the World Climate Research Programme's Working Group on Coupled Modelling, which led the design of CMIP6 and coordinated the work, and also individual climate modelling groups (listed in Supplementary Table 1) for their effort in model simulations and projections.

Author contributions

W.C. conceived the study. W.C., F.J., A.S. and L.W. wrote the initial manuscript. F.J., S.L., A.P., B.G., B.N. and G.W. conducted the analysis. T.G., Y.Y., D.F., G.A.M., M.J.M. and all authors reviewed, edited and improved the paper.

Competing interests

The authors declare no competing interests.

Additional information

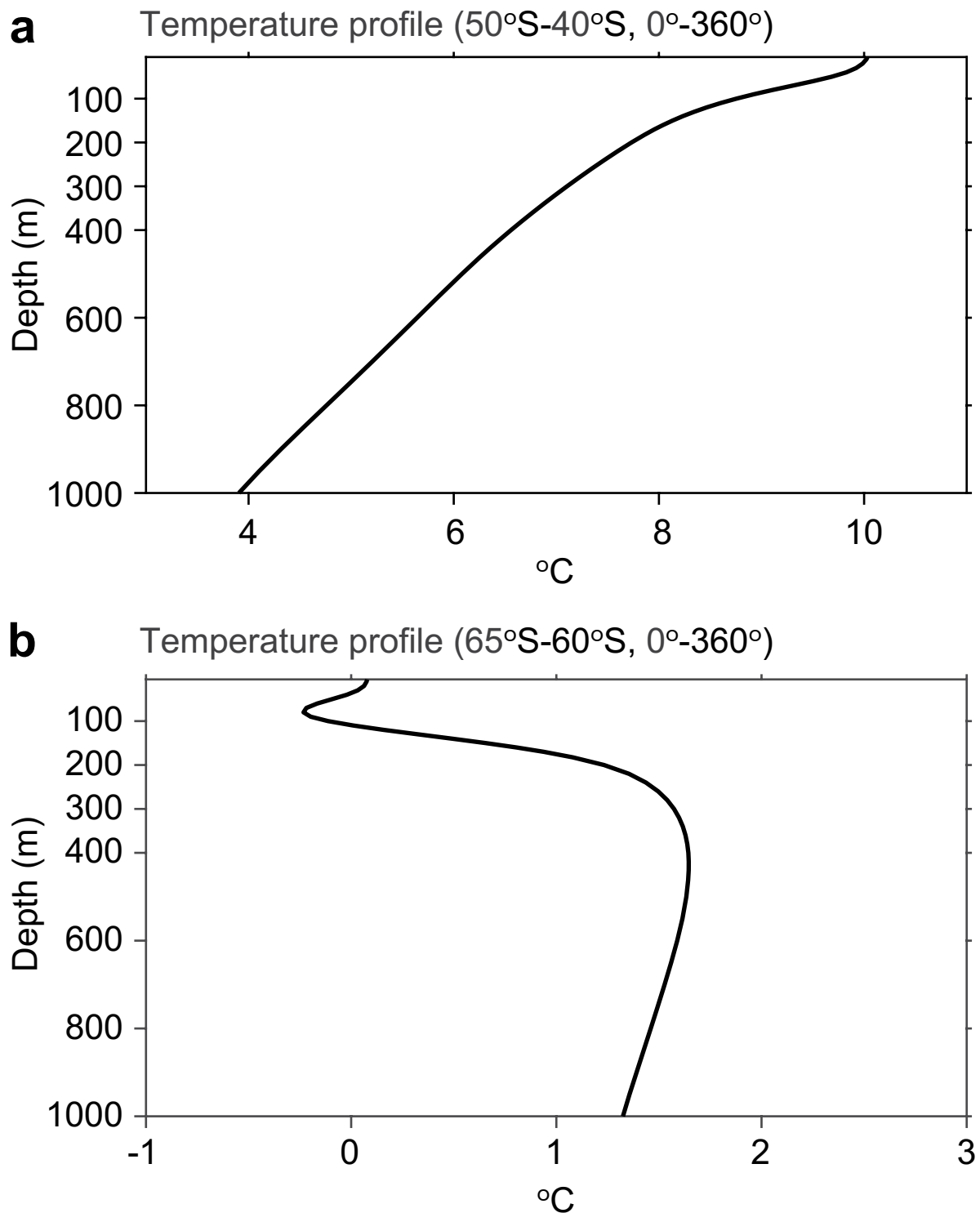
Extended data is available for this paper at <https://doi.org/10.1038/s41558-023-01610-x>.

Supplementary information The online version contains supplementary material available at <https://doi.org/10.1038/s41558-023-01610-x>.

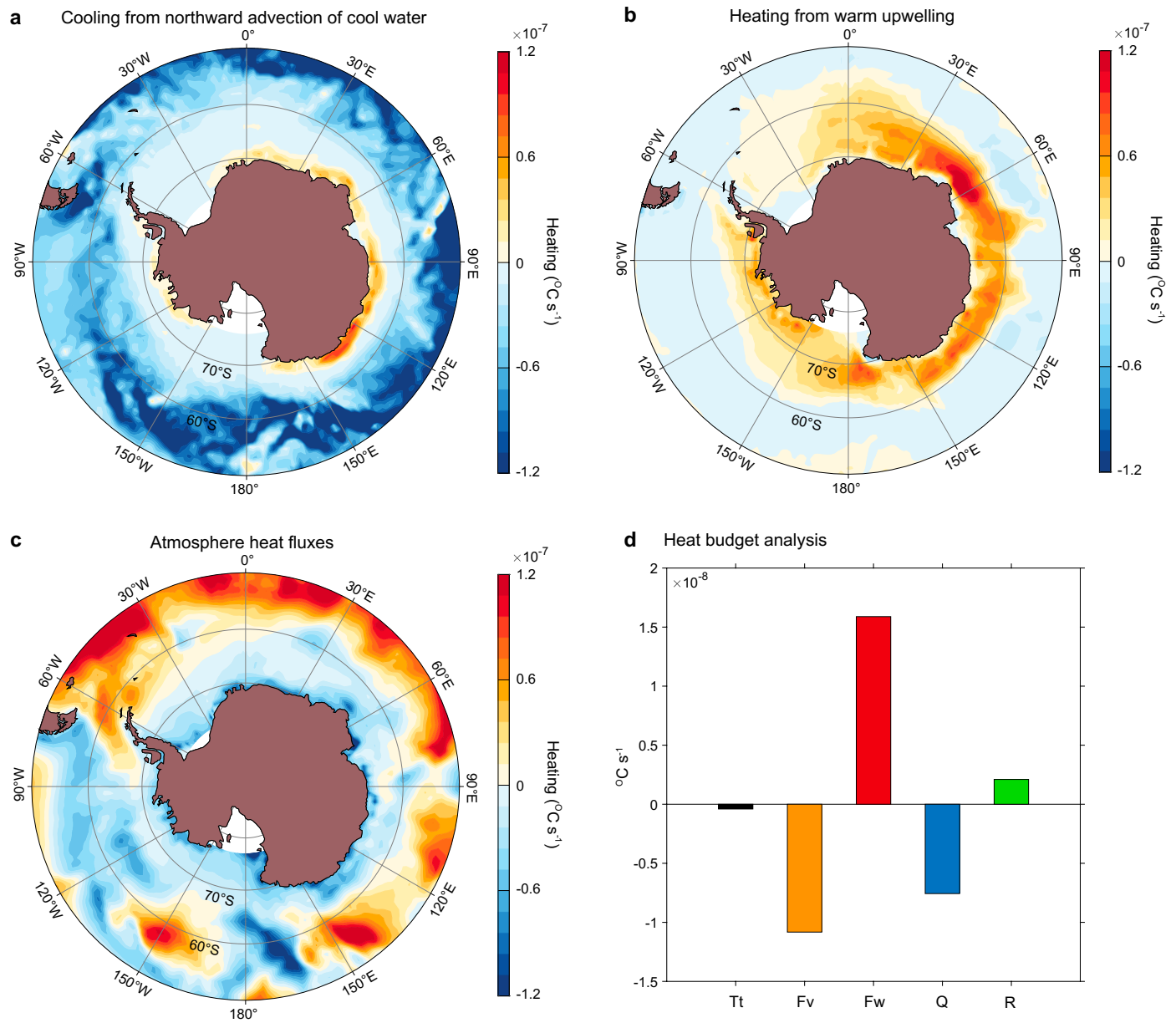
Correspondence and requests for materials should be addressed to Wenju Cai or Lixin Wu.

Peer review information *Nature Climate Change* thanks Shuanglin Li and the other, anonymous, reviewer(s) for their contribution to the peer review of this work.

Reprints and permissions information is available at www.nature.com/reprints.

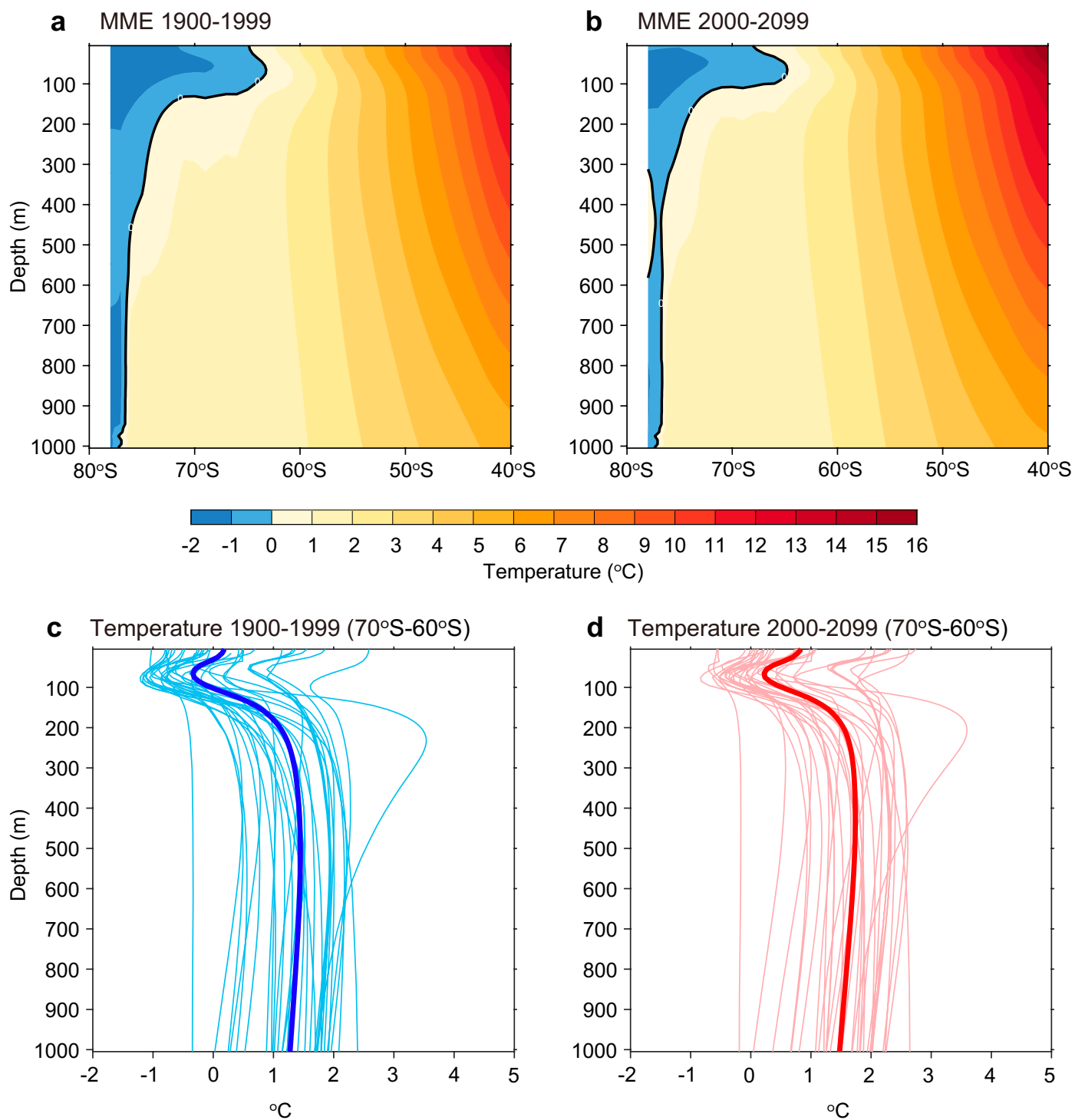


Extended Data Fig. 1 | Observed profiles of annual mean ocean temperatures. (a, b) Vertical profiles of ocean temperatures (°C) averaged over 50°S-40°S, 0-360° and 65°S-60°S, 0-360°, respectively, and over 2004-2020. Ocean temperature data are from the Argo program gridded by Scripps Institution of Oceanography¹.



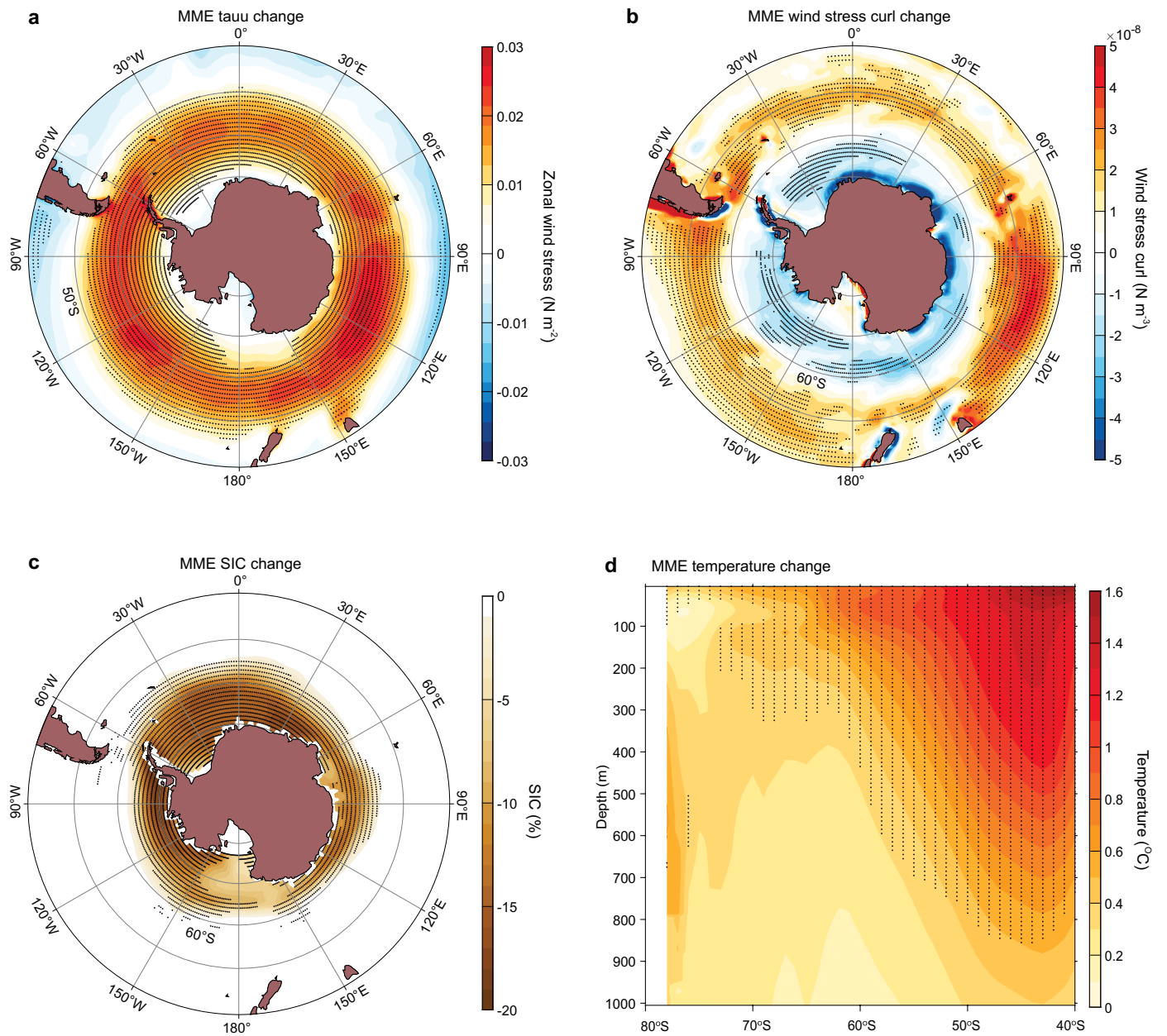
Extended Data Fig. 2 | Observed imprints of two distinctive Southern Ocean upwelling pathways. Spatial pattern of (a) meridional advection by Ekman flows over the upper 100 m ocean ($^{\circ}\text{C s}^{-1}$), featuring cooling north $\sim 60^{\circ}\text{S}$ where upwelled water is colder than the surface water, (b) vertical advection across the 100 m depth by Ekman upwelling, featuring subsurface ocean heating ($^{\circ}\text{C s}^{-1}$) around Antarctica (poleward $\sim 60^{\circ}\text{S}$), where upwelled water is warmer than the

surface water, and (c) air-sea net heat flux ($^{\circ}\text{C s}^{-1}$; positive downward into the ocean). (d) Full heat budget terms (See ‘Observations’ in Methods) based on a dynamically consistent ocean reanalysis product³⁶ for the upper 100 m ocean poleward 60°S averaged over the 1979–2015 period, showing temperature change Tt , contributions from meridional advection Fv , vertical advection by warm upwelling Fw , air-sea flux Q and residual R .



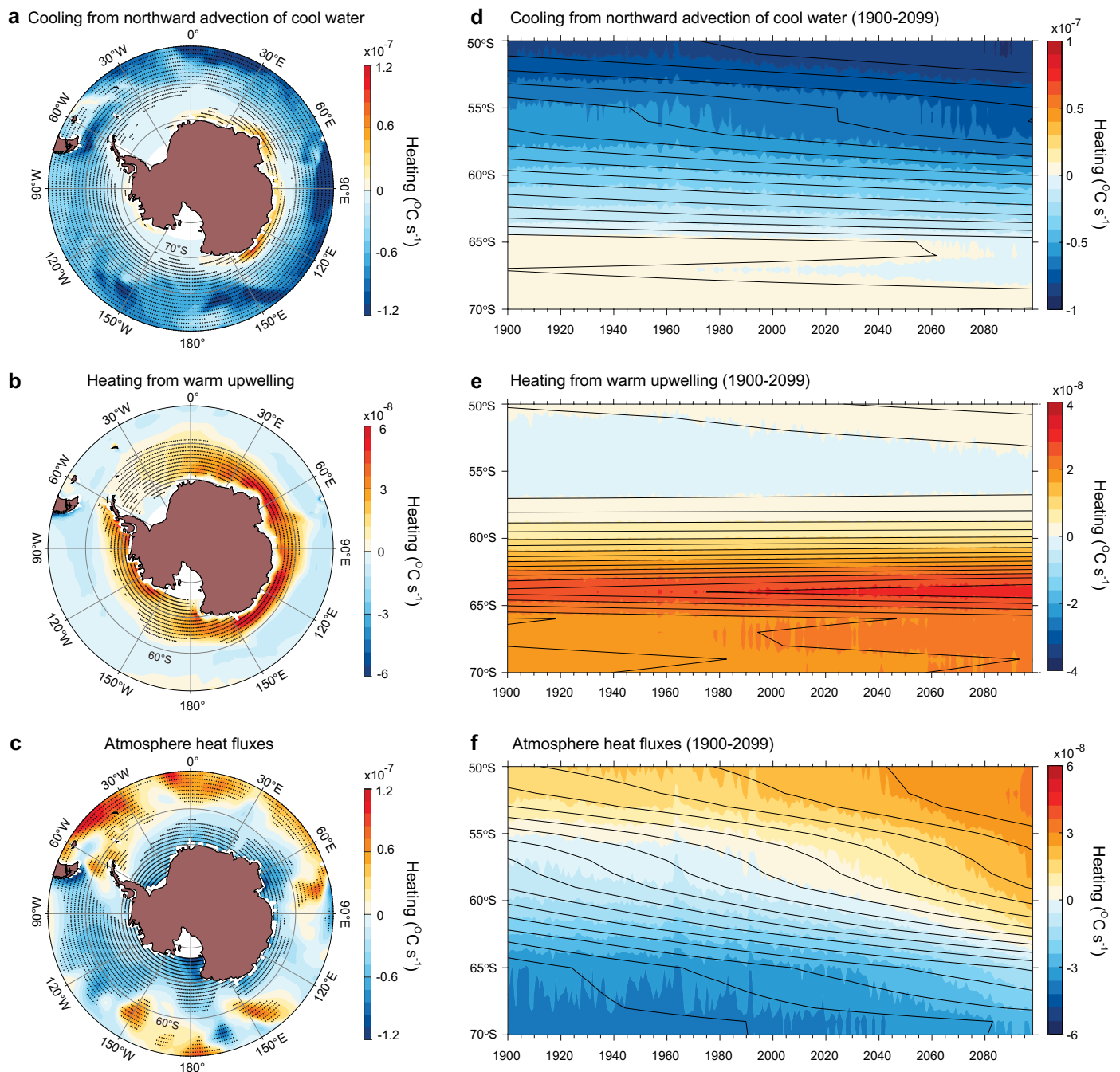
Extended Data Fig. 3 | Simulated vertical ocean temperature profiles. (a, b) Multi-model ensemble average of zonal mean (0–360°) temperature for the 20th (1900–1999) and 21st (2000–2099) century, respectively. **(c, d)** Vertical profiles of ocean temperature averaged over the 70°S–60°S, 0–360° area for the 20th

(1900–1999) and 21st (2000–2099) century, respectively. Light lines in **(c)** and **(d)** indicate individual CMIP6 models, and bold lines indicate the multi-model ensemble mean.



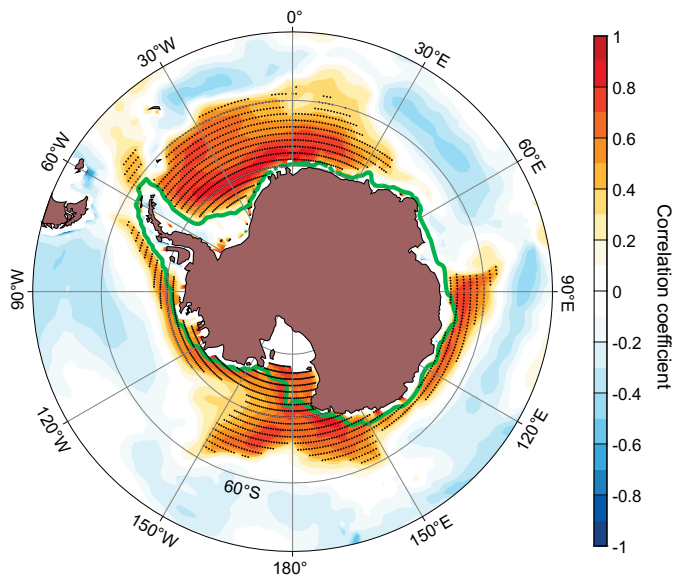
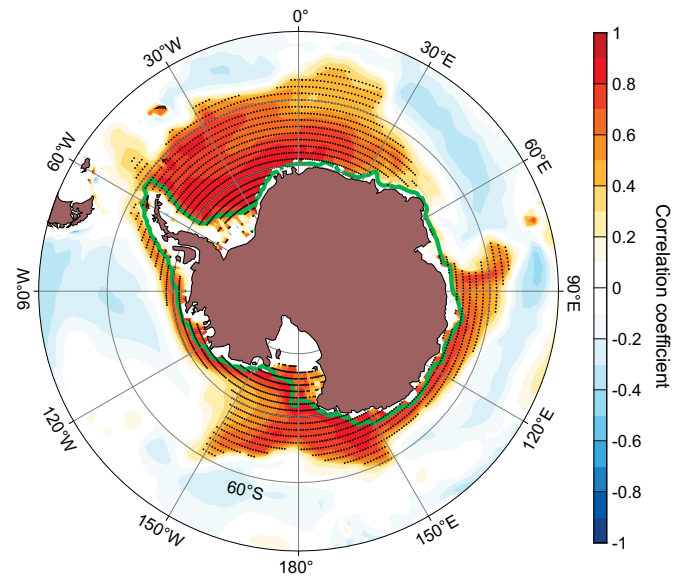
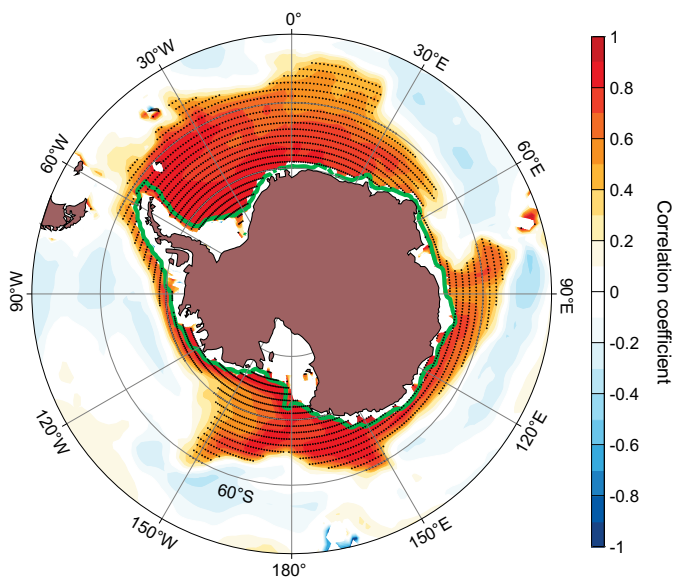
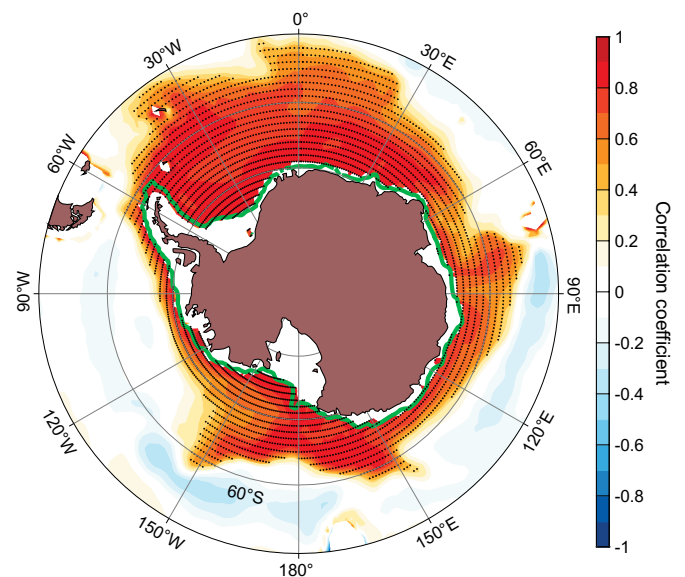
Extended Data Fig. 4 | Simulated circulation changes. Multi-model ensemble mean changes between the 20th (1900–1999) and 21st (2000–2099) century in (a) zonal wind stress (tau; N m^{-2}), (b) wind stress curl (N m^{-3}), (c) sea ice

concentration (SIC; %), and (d) zonally-averaged (0–360°) temperature (°C). Dotted areas indicate that the differences are statistically significant above the 95% confidence level determined by a two-sided Student’s *t* test.



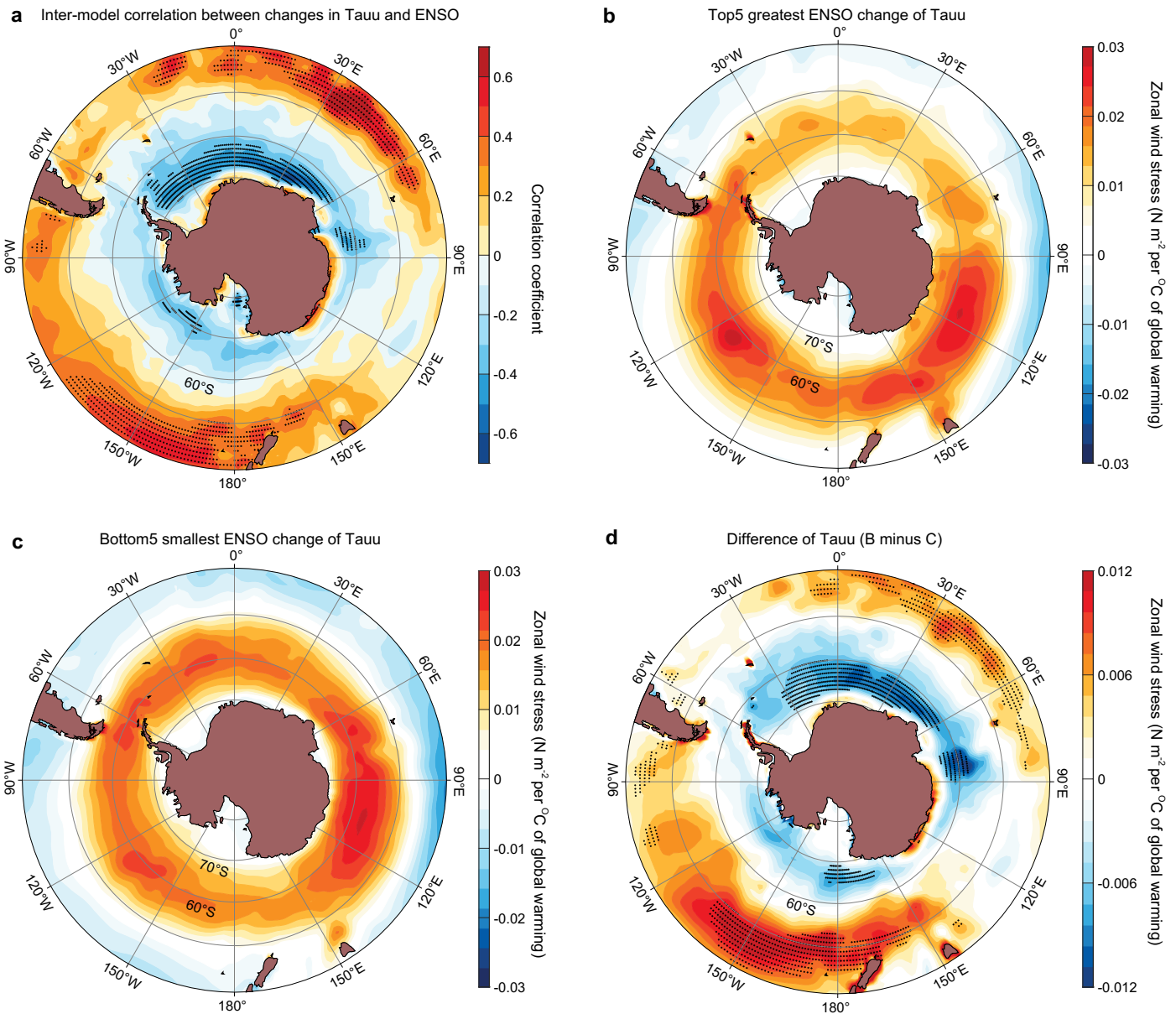
Extended Data Fig. 5 | Simulated two distinctive wind-driven Southern Ocean upwelling pathways and their evolutions. Shown are from a multi-model ensemble average. **(a)** 20th century climatology of northward advection by Ekman meridional velocity ($^{\circ}\text{C s}^{-1}$), generating a cooling north of $\sim 60^{\circ}\text{S}$ where upwelled water is colder than the surface water. **(b)** 20th century climatology of subsurface ocean heating by Ekman upwelling ($^{\circ}\text{C s}^{-1}$) around Antarctica (south of $\sim 60^{\circ}\text{S}$), where upwelled water is warmer than the surface water. **(c)** 20th century climatology of atmospheric heat fluxes ($^{\circ}\text{C s}^{-1}$; positive downward). **(d-f)**,

Evolution of annual mean (April to March) **(d)** northward advection by Ekman meridional velocity ($^{\circ}\text{C s}^{-1}$), **(e)** subsurface ocean heating by Ekman upwelling ($^{\circ}\text{C s}^{-1}$), and **(f)** atmospheric heat flux ($^{\circ}\text{C s}^{-1}$). Contours in **(d-f)** indicate isolines of a linear trend fit in each latitude. Dotted areas in **(a-c)** represent annual mean greater than one standard deviation of the inter-model spread in amplitude. A westerly poleward intensification drives an increased cooling trend north of $\sim 60^{\circ}\text{S}$, but a warming trend around Antarctica, against the backdrop of increasing atmospheric heat fluxes into the ocean.

a Temperature (200–400m) change and shelf water warming**b** Temperature (400–600m) change and shelf water warming**c** Temperature (600–800m) change and shelf water warming**d** Temperature (800–1500m) change and shelf water warming

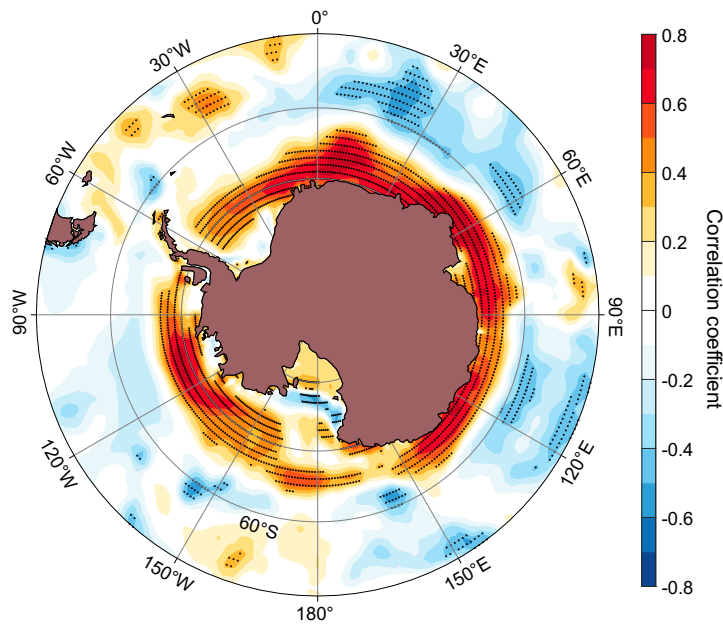
Extended Data Fig. 6 | Shelf water warming and temperature change at various depths. Inter-model correlation between changes in shelf water temperature ($^{\circ}\text{C}$ per $^{\circ}\text{C}$ of global warming; averaged over -2° to $+1^{\circ}$ latitude from 1000 m isobath, 400–1500 m) and changes in temperature ($^{\circ}\text{C}$ per $^{\circ}\text{C}$ of global warming) averaged over (a) 200–400 m, (b) 400–600 m, (c) 600–800 m

and (d) 800–1500 m. Green line indicates the multi-model ensemble mean 1,000-m isobath at each longitude. Dotted areas indicate where the correlation coefficients are statistically significant above the 95% confidence level determined by a two-sided Student's t test.

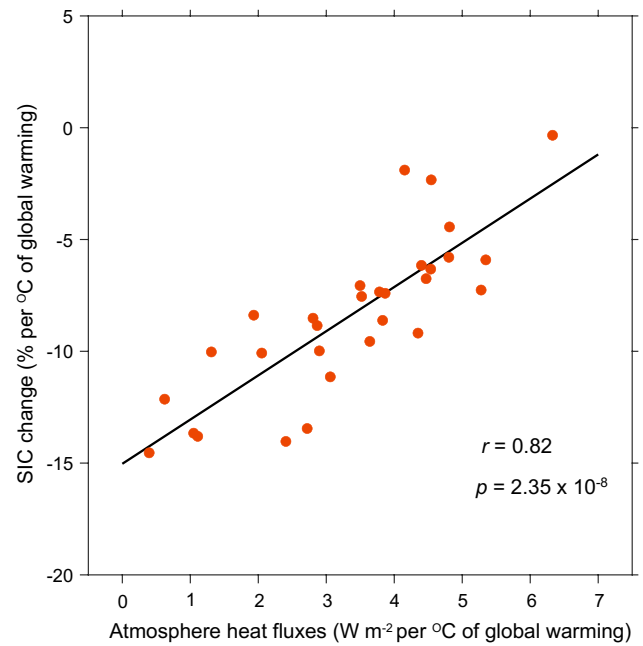


Extended Data Fig. 7 | Changes in zonal winds affected by ENSO response to greenhouse warming. (a) Inter-model correlation between changes in zonal wind stress (tau; $N\ m^{-2}$ per $^{\circ}C$ of global warming) and changes in standard deviation of DJF Niño3.4 index ($^{\circ}C$ per $^{\circ}C$ of global warming). Zonal wind stress changes ($N\ m^{-2}$ per $^{\circ}C$ of global warming) in (b) the top-5 models with greatest ENSO variability

change, (c) bottom-5 models with smallest ENSO variability change and (d) the difference between the two groups of models (b minus c). Dotted areas in (a) and (d) indicate the correlation or differences that are statistically significant above the 95% confidence level determined by a two-sided Student's *t* test.

a Inter-model correlation between heat flux and SIC change

Extended Data Fig. 8 | Greater sea ice reduction despite a smaller increase in atmospheric heating. Inter-model correlation of changes between the 21st and 20th century in sea ice concentration (SIC) averaged over 70°S–60°S (% per °C of global warming) with grid-point changes in air-sea net heat flux into the upper 100 m ocean (W m^{-2} per °C of global warming); dotted areas indicate correlation coefficients that are statistically significant above the 95% confidence level

b Inter-model correlation

determined by a two-sided Student's *t* test. **(b)** Inter-model correlation between changes in SIC and changes in air-sea heat flux, both averaged over 70°S–60°S and scaled by the increase in global mean SST; a linear fit is displayed together with correlation coefficient *r* and *p* value. A smaller increase in heat flux into the ocean is associated with a greater sea ice reduction (a positive correlation).